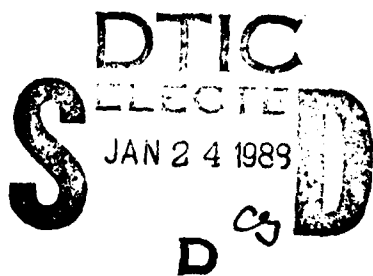## LaJolla INSTITUTE

CENTER FOR STUDIES OF NONLINEAR DYNAMICS
7855 FAY AVENUE, SUITE 320
LA JOLLA, CALIFORNIA 92037

LJI-88-P-484

DTIC FILE COPY
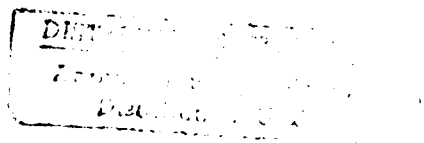
Comparison of Computed SAR Focus-Setting Curves with Model Predictions

DTIC
SELECTED
JAN 2 4 1989
D

R.J. DeWitt

F.S. Henyey

J.A. Wright

Center for Studies of Nonlinear Dynamics

La Jolla Institute

7855 Fay Avenue, Suite 320

La Jolla, California 92037

Comparison of Computed SAR Focus-Setting Curves with Model Predictions

R.J. DeWitt

F.S. Henyey

J.A. Wright

Center for Studies of Nonlinear Dynamics

La Jolla Institute

7855 Fay Avenue, Suite 320

La Jolla, California 92037

Abstract

In this paper we analyze data from the TOWARD experiment to compute experimental SAR focus-setting curves for data obtained from two different altitudes. The purpose of the paper is to compare these experimental curves with the model predictions of Schult, Henyey, and Wright (1988), which is a companion paper to this one. The model predicts that the optimal focus-setting velocity for azimuthally-traveling long surface waves occurs at one-half of the phase speed of the dominant wave. The computed curves are in good agreement with this prediction; they simultaneously rule out the possibility that the optimal focus-setting velocity occurs at the phase velocity or the orbital velocity of the wave. An important part of the paper involves the manner in which the data is analyzed. We show that analysis of the full two-dimensional spectrum of the SAR image guarantees that the full signal of interest is included in the processing and provides a consistent technique by which background noise can be removed from the signal.

1. Introduction

There has been some controversy in the SAR community as to the proper focus-setting velocity to be used in processing SAR data for a time- dependent image like the ocean surface. The argument concerns which of the several velocities associated with the surface is to be subtracted from the aircraft velocity in the SAR processing to obtain the optimally-focused image. One popular model favors the use of phase velocity of the long waves being imaged, while another favors the orbital velocity associated with the waves.

In a companion paper to this one, Schult, Henyey, and Wright (1988) have developed a model of SAR imaging which predicts that, while both the phase and orbital velocities are important in establishing the optimal focus setting, the two velocity effects combine together to give an optimal focus-setting velocity at just half of the phase velocity of the azimuthally-directed long waves being imaged when the local current (e.g., the orbital velocity of the long wave) is small compared to the phase velocity.

The purpose of this paper is to show that the prediction of the model is in good agreement with focus-setting curves computed from actual SAR data, specifically from L-band SAR images obtained during the TOWARD experiment, which include images of surface swell that can be used to determine relative focusing levels as a function of the focus-setting velocity used to process the SAR image. We obtained SAR-processed data in the form of a sequence of data files corresponding to different focus-setting velocities. Each data file represents one picture of the surface, SAR-processed at a particular focus-setting velocity. In order to compare with the theoretical prediction, we compute the noise-reduced energy associated with the dominant swell in the picture. Because the theory predicts both the optimal focus-setting velocity and the relative energies associated with de-focused images, we can use the computed energy as a function of focus-setting velocity to compare with the model prediction. We find good agreement between the model prediction and the computed focus-setting curves. The agreement is good enough to rule out the possibilities of optimal focus-setting velocities occuring at either the phase velocity or the orbital velocity of the waves for this data set.

The other contribution made by this paper is to demonstrate the importance of using a full two-dimensional spectrum when performing spectral analysis of the SAR data. Not only does examination of the full spectrum lead to a precise identification of the

wavevectors of interest but also provides a consistent way to remove the background noise (speckle) contribution from the signal, to the extent to which that is possible. Our technique for computing the noise-reduced energy in a signal is to first examine the two-dimensional spectrum and locate the region associated with the signal of interest. We compute the energy-weighted average wavevector of the signal to define the center of the region, and then compute the total energy associated with a circular region centered on the average wavevector. The effective radius of the region is set by the width of a gaussian that is used to weight the energies.

Computing the energy in a region of k-space rather than at a single point also provides a systematic way to reduce the noise contribution. We introduce a technique for projecting the k-space signal associated with one focus setting onto the signal at the optimal focus setting. We show that this technique can substantially reduce the noise level in the computed energies.

In Section 2 we describe the data being processed in this paper and introduce some basic symbols and conventions. We follow in section 3 with a description of the pre-processing done on the data to eliminate biases in the raw data. In section 4 we discuss the spectral analysis of the data, including the computation of the average wavevector of the signal, the total energy of the signal, and the noise-reduced energy of the signal. This section includes the description of the projection method. We also identify the regions of high and low spectral activities with the open and shadow regions, respectively, created by the local islands off the coast of Southern California. Section 5 compares the computed focus-setting curve with that predicted by the model and finds good agreement between the two. In section 6 we display a computed focus-setting curve for data from essentially the same experimental situation except that the aircraft was at a lower altitude. The focus-setting curve is seen to be consistent with the predictions of the model equation and the projection method.

2. Description of the data

We were provided with SAR data in the form of three tapes, each containing a sequence of 15 floating-point-format data files. Each data file corresponds to an image processed at one focus-setting velocity. In this paper we refer to each such file as a "picture". Details of the data gathering and preparation can be found in Tajirian (1987). The first two tapes, referred to as AXCMF003 and AXCMF006 in that report, both

correspond to the same physical situation; the only difference in them is that the focus-setting velocities were chosen at different values. Both tapes are for a region of the ocean near the NOSC Tower imaged from an aircraft flying at 38,000 feet during the "Leg 1" portion of the TOWARD experiment. The depth of the water at the center of the chosen region is 60 m. All of the data files in this study contained 256 rows of 256 pixels each. Each pixel represents the SAR intensity of a region of ocean surface 10.98 m square. Tape AXCMF003 is a sequence of pictures with focus-setting velocities ranging from -19.25 m/s to +19.25 m/s in equal steps of 2.75 m/s. Tape AXCMF006 is a similar sequence with velocities ranging from -25.67 m/s to +25.67 m/s in steps of 3.67 m/s. Since focus-setting curves from both tapes are presented in Tajirian (1987), we analyzed both tapes in order to make comparisons with the results presented in that report. The third tape made available to us is identical to tape AXCMF006 in all respects except that that data was taken with the aircraft flying at 20,000 feet instead of 38,000 feet. We note here that all of the calculations shown in sections 3 and 4 of this paper use the data files from tape AXCMF006, since they span a broader ranger of focus-setting velocities. In section 5, where we compare the computed curves with the model prediction, we show results from both tapes.

A typical picture is shown in Figure 1, using a linear gray scale to represent intensity. The horizontal direction in the picture represents the azimuthal direction of the SAR and the vertical direction represents the range direction. Visible in the picture are a sequence of nearly vertical, parallel lines that are due to narrow-band surface waves traveling nearly along the azimuthal direction. The data for the picture has been processed to eliminate biases, as described in the next section, and has then been passed through a low-pass filter to enhance the viewing of the surface waves for this figure only.

In subsequent mathematical descriptions of the data we will refer to the intensity of a particular pixel by $I_{v_f}(x,y)$, where the subscript v_f refers to the focus-setting velocity used in processing the original SAR data, and x and y refer to the azimuthal and range directions of the SAR, respectively. The origin of the coordinate system is chosen to be at the upper left corner of the picture; x increases to the right and y increases downward.
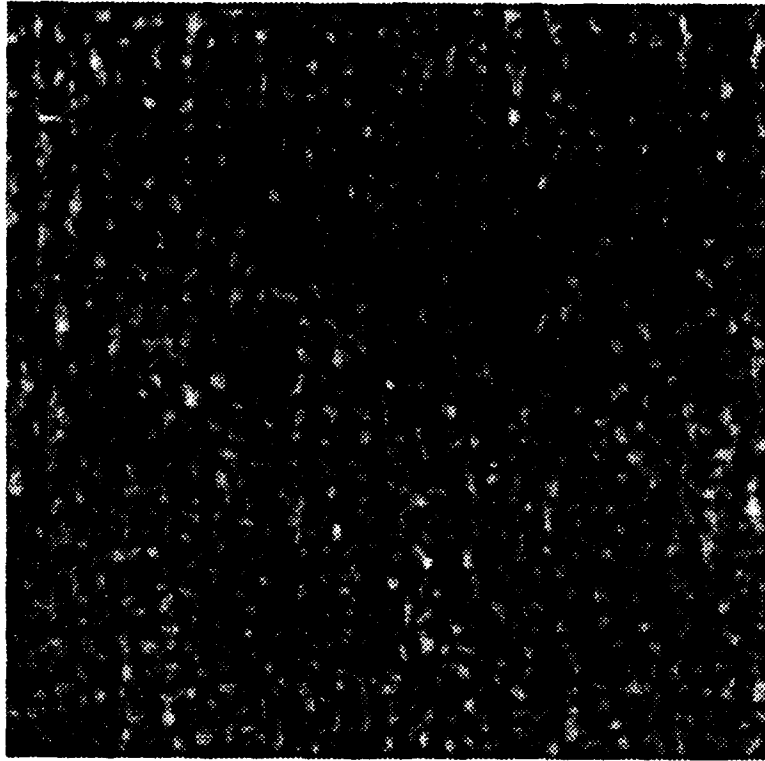
Figure 1. A linear gray scale representation of one of the SAR images. The images corresponds to a focus-setting velocity of 5.5 m/s. Visible in the picture are a sequence of nearly vertical, parallel lines that represent surface waves traveling nearly along the azimuthal direction.

3. Eliminating Biases from the Data

Before performing spectral analysis, the data was processed to eliminate biases that would introduce spurious components in the spectrum. These sources of bias included (1) a sequence of three spurious rows of data at the bottom of each picture, (2) a systematic decrease in the intensity of each picture from the top to the bottom, (3) a systematic increase in the overall dc level of successive pictures as the focus-setting velocity is increased.

3.1 Fixing spurious rows

The original data contained three spurious rows at the bottom of each picture, identifiable as such by containing either identically zero values across the row or values that were unrealistically below those for a typical row. In order that these rows would not introduce spurious high wavenumber signals into the spectrum due to the sudden drop in intensity level in the y direction, this data should be eliminated. However, having the number of rows equal to a power of two has obvious advantages for performing fast Fourier transforms. We therefore re-defined the intensities in the last three of the 256 rows to be equal to the corresponding values in row 253. This provided an arbitrary but smooth way to extend each picture to 256 rows while eliminating the possibility of introducing spurious high wavenumber components in the spectrum.

3.2 Detrending

We corrected for the trend toward decreased intensity from top to bottom in each picture by normalizing each row by a measure of its mean intensity. To that end we define the row-intensity of the picture by

$$I_{v_f}(y) \equiv \sum_x I_{v_f}(x,y) \tag{1}$$

This gives us a measure of the overall intensity level at a given vertical position. We took as a representative picture the data associated with focus-setting velocity $v_f = 14.7$ m/s. We computed $I_{(14.7m/s)}(y)$ and then generated an analytical fit to the resulting curve. The data turned out to be well fit by a single exponential curve that we call the detrending function, $I_D(y)$:

$$I_D(y) = c_0 e^{-c_1 y} \tag{2}$$

The fit yielded $c_0 = 4.1 \times 10^{-3}$ and $c_1 = 3.3 \times 10^{-3}$. In Figure 2 the jagged curve represents

$I_{v_f}(y)$ for $v_f = 14.7 m/s$ and the solid curve represents $I_D(y)$. Given $I_D(y)$ it is then a simple task to detrend each picture, which we do by dividing all values in a given row by the value of I_D for that row:

$$I'_{v_f}(x,y) = I_{v_f}(x,y) / I_D(y) \qquad (3)$$

Using a smooth curve for the detrending function eliminates the possibility of introducing spurious high-wavenumber contributions to the modified data. We also emphasize here that we used exactly the same detrending function for each picture rather than generating a different function for each. This further eliminates the possibility of either creating spurious trends or destroying bonafide trends between pictures. For comparison, the curve $I'_{v_f}(y)$ is shown in Figure 3 for $v_f = 14.7$ m/s. The curve shows a flat row-intensity function, indicating that the vertical bias in the data has been eliminated. The curves for all other values of v_f are quite similar.

3.3 Eliminating dc bias

The data also show a monotonic increase in the dc level of the spectrum as a function of focus-setting velocity. If we denote the two-dimensional Fourier transform of a picture by

$$\tilde{I}_{v_f}(\vec{k}) = \int d^2\vec{x}\, e^{i\vec{k}\cdot\vec{x}} I_{v_f}(\vec{x}) \qquad (4)$$

then the dc level is just $\tilde{I}_{v_f}(0)$. Figure 4 shows the dc level of the raw data as a function of v_f. Left uncorrected, this trend would skew later focus-setting curves. To eliminate the trend we divide all of the values of a given picture by the dc value of the picture:

$$I''_{v_f}(\vec{x}) = I'_{v_f}(\vec{x}) / \tilde{I}_{v_f}(0) \qquad (5)$$

Of course since the Fourier transform is linear, it doesn't matter whether the division is actually done in x-space or k-space.

Having now done the preprocessing necessary to eliminate biases from the pictures, we will assume that all subsequent references to intensities in this paper refer to unbiased intensities and will henceforth drop the primes on the intensity function.
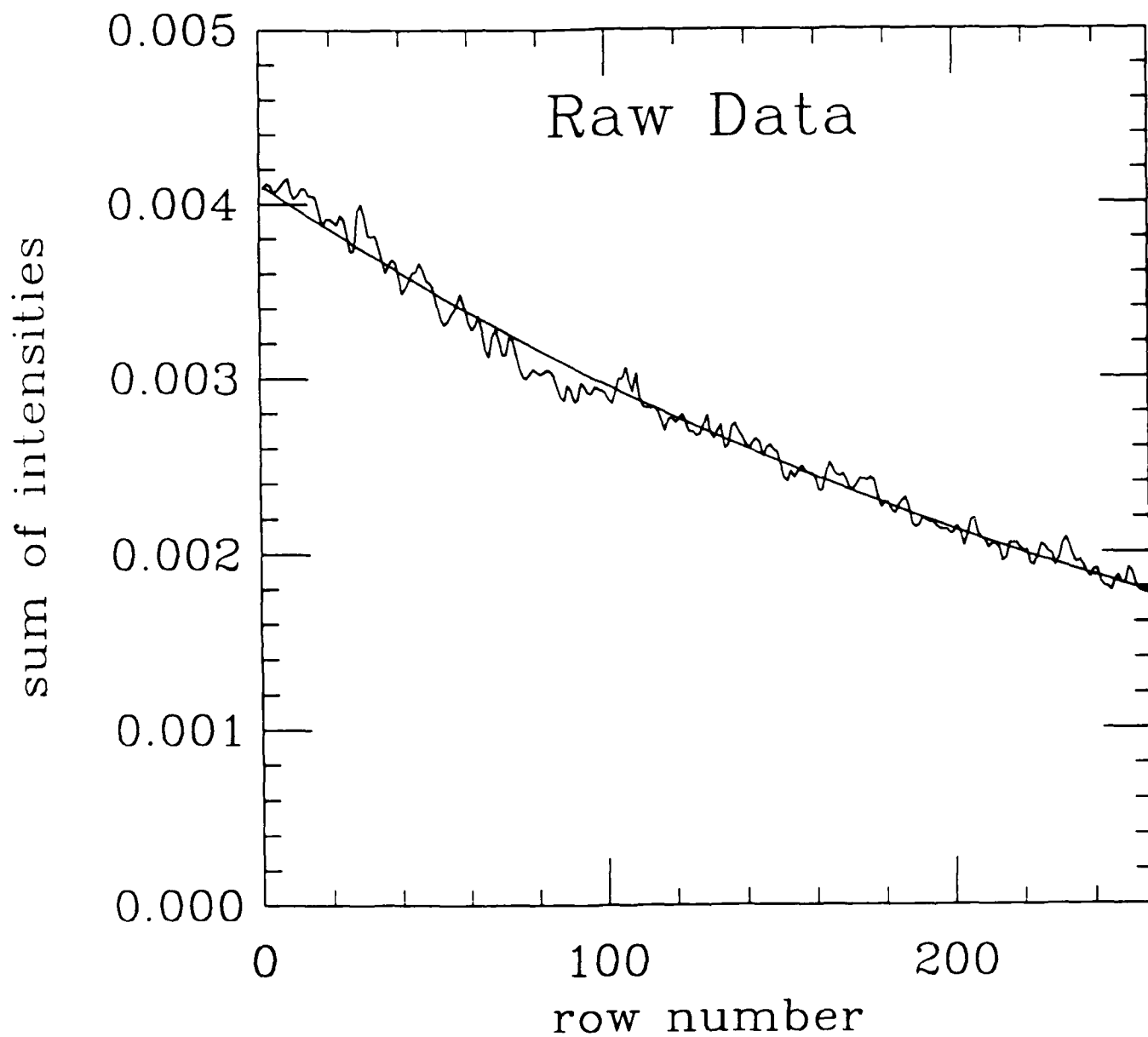
Figure 2. The row-intensity of one of the SAR images. The jagged curve represents the actual row-intensity of the image and the solid curve is an analytic fit to the data, which is used as the detrending function.
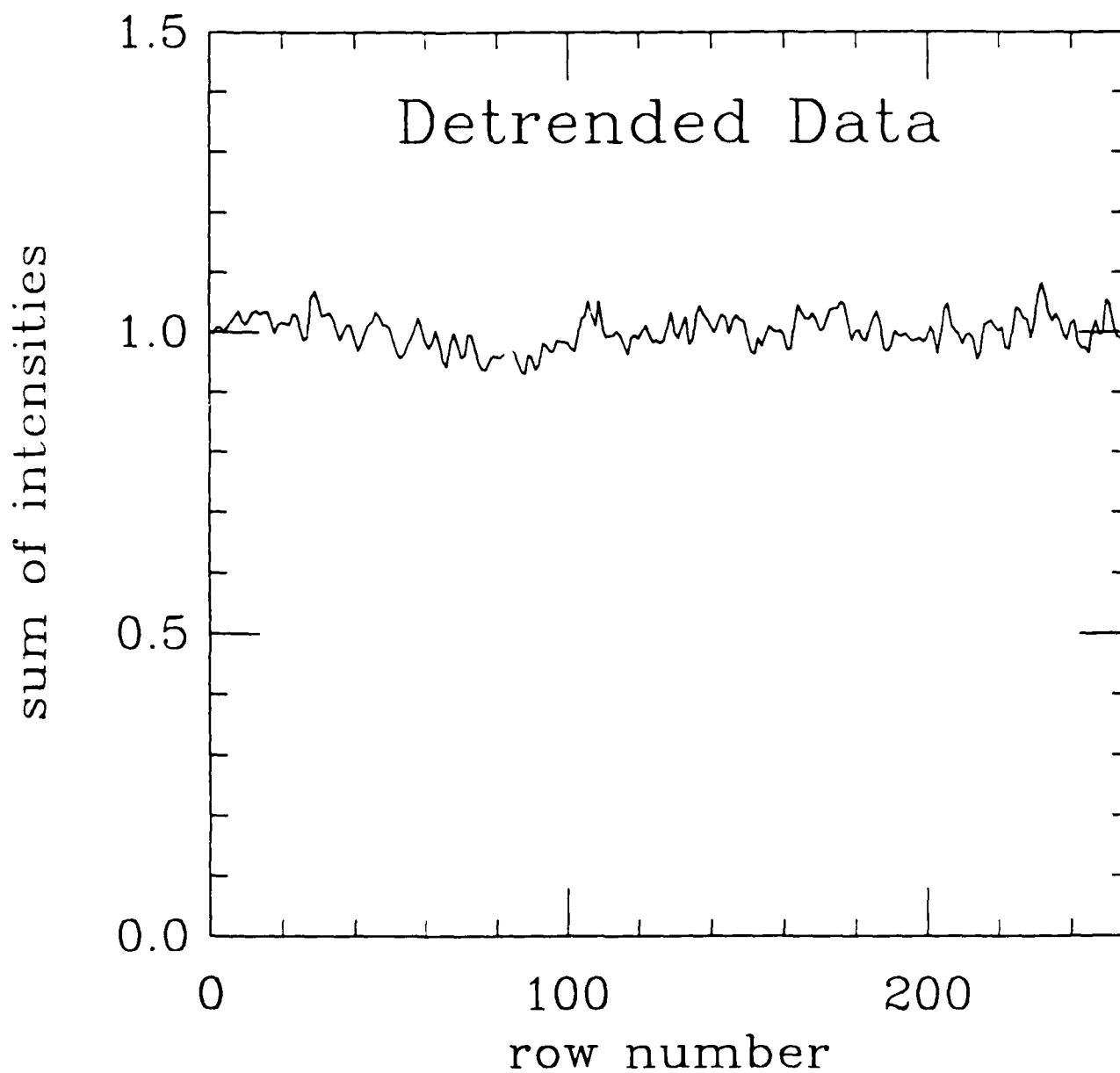
7-1-'88

Figure 3. The row-intensity of a detrended SAR image, revealing that the trend toward lower intensity with increasing row number has been removed.
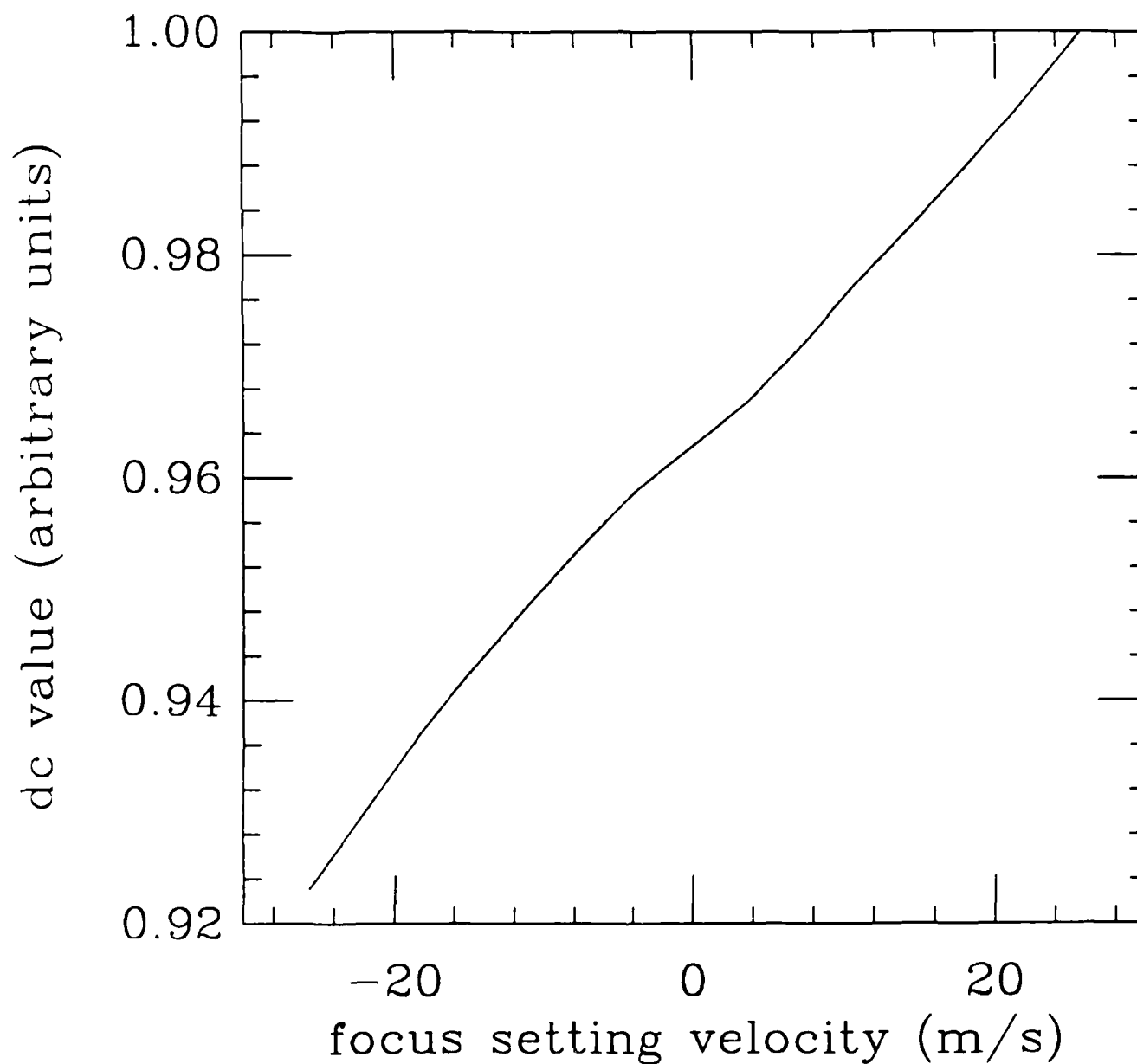
7-1-'88

Figure 4. The DC level of each SAR image as a function of its focus-setting velocity. Left uncorrected, this DC trend would skew later focus-setting curves to higher values at larger focus-setting velocities; the DC value is divided out of all energy calculations.

4. Spectral Analysis

We performed a two-dimensional finite Fourier transform of each picture. A good understanding of the features in a picture can be obtained by examining the two-dimensional spectrum, defined as

$$E_{v_f}(\vec{k}) \equiv |\tilde{I}_{v_f}(\vec{k})|^2 \tag{6}$$

A typical 2-D spectrum is shown in Figure 5, which represents a linear gray scale plot of E for $v_f = 7.3$ m/s. The smallest value is represented by white and the largest value by black. The origin is at the center left edge, with a small region around $\vec{k} = 0$ artificially set to zero for display purposes. The horizontal axis represents k_x and the vertical axis k_y, with positive k_y downward. Only the relatively low wavenumber portion of the spectrum is shown; the high wavenumber region contains only noise. In addition, only the positive k_x quadrants have been plotted. The negative k_x quadrants are just reflections of these two quadrants, according to

$$E_{v_f}(-\vec{k}) = E_{v_f}(\vec{k}) \tag{7}$$

which follows from the fact that $I_{v_f}(\vec{x})$ is real. The k values in the figure are in units of Δk, defined by

$$\Delta k \equiv \frac{2\pi}{L} = 2.24 \times 10^{-3} m^{-1} \tag{8}$$

where $L = (10.98m / pixel)(256 pixels) = 2810m =$ width (and height) of the picture.

The dominant swell component in the spectrum is evident at $\vec{k} = (23, 2)$ and the immediately surrounding region. Other waves can be seen around the regions (4,-4) and (19,-8). It should be clear from this spectral plot that, even though it was the intention during the "Leg 1" portion of the experiment that the aircraft fly exactly along the direction of the dominant visible swell, it would be a mistake to make this assumption in doing spectral analysis, since the assumption is equivalent to considering only wavevectors whose k_y component is zero. Clearly most of the activity does not lie exactly on the k_x axis, however, so analyzing only the $k_y = 0$ signal misses the major part of the dominant wave.

4.1 Average $\vec{k}$ of the swell region

By far the largest signal in the spectrum is the band associated with the nearly azimuthally travelling surface swell. The spectrum has a maximum value in this region at the wavenumber $\vec{k} = (23,2)$, again in units of Δk. In order to get a quantitative measure of the center of this region in k-space we compute the weighted average value of $\vec{k}$ in the region $16 \le k_x \le 30$ and $-6 \le k_y \le 8$. The region was selected by a visual examination of the two-dimensional spectrum to include the significant wavevector components of the swell. The weighted average is defined by

$$\langle \vec{k} \rangle_{v_f} \equiv \frac{\sum_{\vec{k}} \vec{k} E_{v_f}(\vec{k})}{\sum_{\vec{k}} E_{v_f}(\vec{k})} \tag{9}$$

where the sums are understood to be restricted to the above stated rectangular region. We chose $v_f = 7.3$ m/s and computed a value $\langle \vec{k} \rangle = (23.1, 1.07)$, which corresponds to a wavelength of 121 m.

4.2 Identification of spectral sources

One interesting aspect of the two-dimensional spectrum shown in Figure 5 is that regions of low activity can be shown to be correlated with the directions of surface-wave shadows from islands off of the coast of Southern California; regions of high activity correspond to the gaps between the islands. The islands involved include San Clemente, San Nicolas, Santa Rosa, and Santa Catalina Islands. Figure 6 is a map of the local ocean region with lines drawn to define the shadow regions. We expect that the closer islands, in particular San Clemente Island and Santa Catalina Island, will have a significant shadowing effect on the swell in the Mission Beach area.

We have computed the angles of each line shown Figure 6 and have transferred these directions to the two-dimensional spectrum shown in Figure 7. In this case the horizontal line (in the k_x direction) corresponds to the nominal aircraft flight direction. For reference, the uppermost line represents due east and the line that drops through the bottom of the figure is due south. In interpreting this figure one should think of each line as being associated with a direction from the indicated island toward the NOSC tower area. Thus, for example, though Santa Catalina Island is north-west of the NOSC tower, waves moving past the the island will approach the tower moving toward the south-east. One
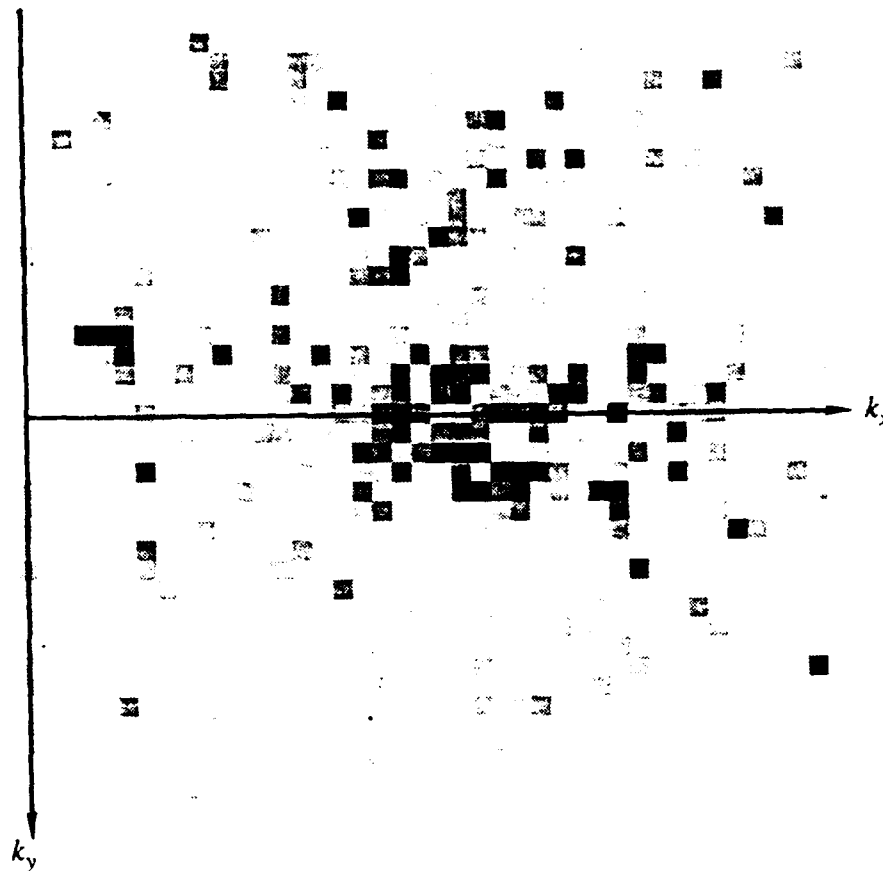
Figure 5. A two-dimensional spectrum for the image $v_f = 5.5$ m/s in a linear gray-scale representation. Larger values are represented by darker boxes. A small region around $\vec{k} = 0$ is artificially blanked out for display purposes. Clearly visible are the components of the major swell located around $\vec{k} = (22, 3) \Delta k$.
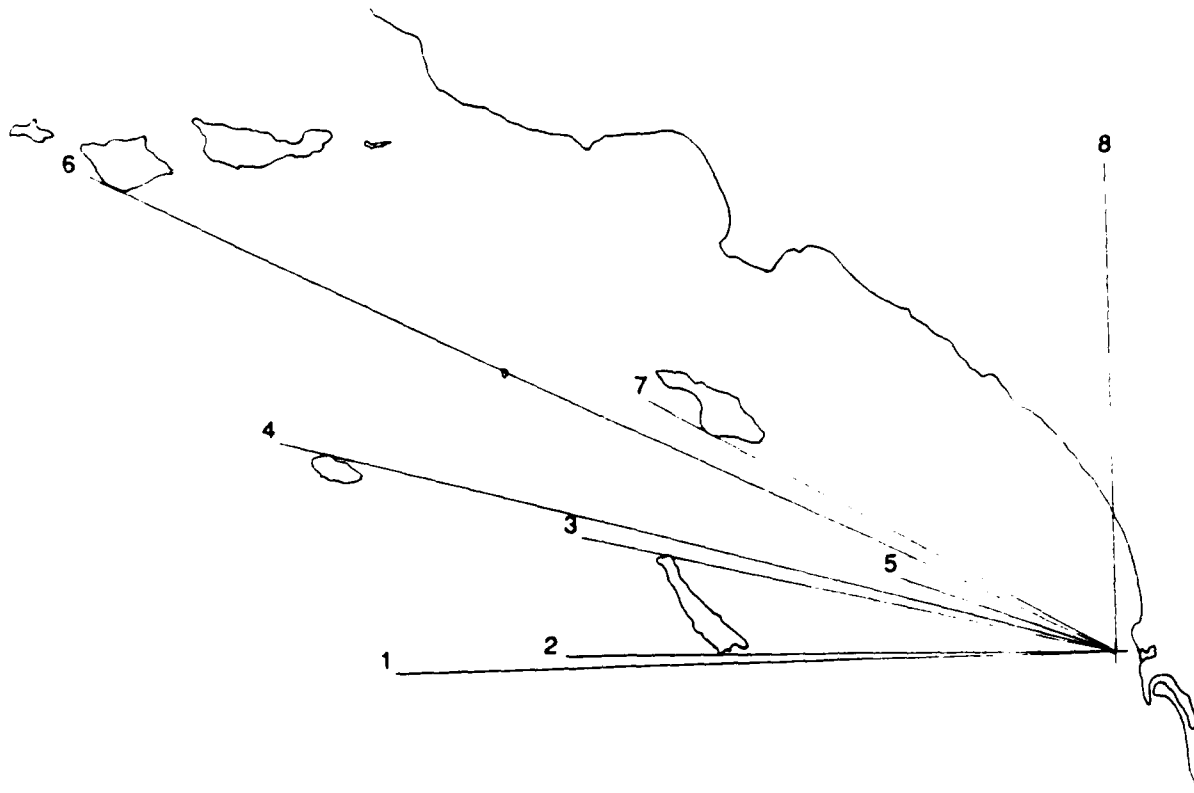
Figure 6. A map of the ocean region near the NOSC tower area. The map is used to compute the angles of shadow regions created by local islands for comparison with the directions associated with low spectral activity.
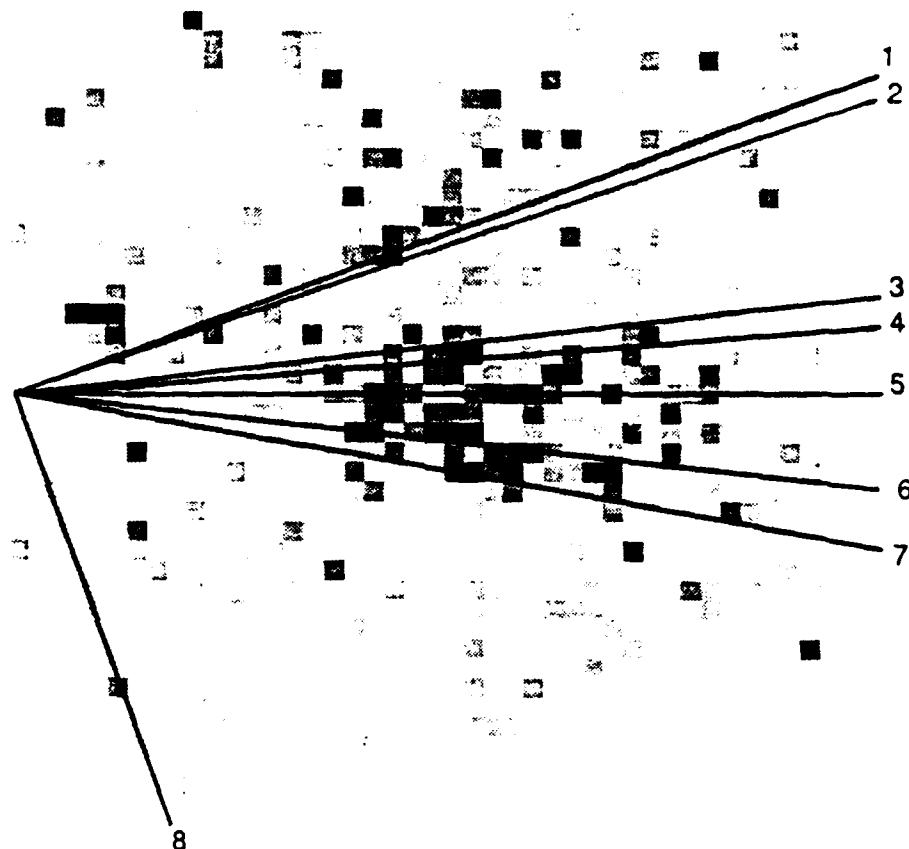
Figure 7. The two-dimensional spectrum from Figure 5 with the directions computed from Figure 6 superimposed. The horizontal line (in the k_x direction) corresponds to the nominal aircraft flight direction. For reference, the uppermost line represents due east and the line that drops through the bottom of the figure is due south. In interpreting this figure one should think of each line as being associated with a direction from the indicated island toward the NOSC tower area. One sees a well-delineated region of low activity between the lines San Clemente North and South and another region of low activity beginning just north of the line associated with Santa Catalina South; high activity is associated with the open region bounded by the directions Santa Rosa South and San Nicolas North; the largest single component, at $(23, 2)\Delta k$, is from the direction connected with the southern tip of Santa Rosa.

can alternatively rotate one of the figures through 180 degrees and align corresponding lines in the two figures. We should point out here that a line drawn through San Nicolas South and the tower area passes through the San Clemente North, so no separate line for San Nicolas South has been included in the picture.

One sees in the Figure 7 a well-delineated region of low activity between the lines San Clemente North and South, indicating that San Clemente Island is an effective barrier to the swell. Another region of low activity begins just north of the line associated with Santa Catalina South, indicating both a shadowing effect of that island and also a low amount of activity associated with waves moving nearly parallel to the coast (from north of Santa Catalina Island). Conversely, the highest activity is from the open region bounded by the directions Santa Rosa South and San Nicolas North; in fact the largest single component, at $(23,2)\Delta k$, is from the direction connected with the southern tip of Santa Rosa. South of the line defined by San Clemente south we see activity increasing again as we move out of the shadow of San Clemente, with significant activity in the regions around (4,-4) and (19,-8), among others.

4.3 Computation of the total energy in the swell

We wish to compare the computed strength of the signal present in each picture. We first compute the total energy associated with the region of the spectrum associated with the major swell component in the picture. In order not to impose a sharp cutoff on the definition of the region, we compute the energy weighted by a gaussian function centered on the average $\vec{k}$ value of the swell, given above as (23.1,1.07). We define the total energy in the swell as

$$E_{v_f}^T \equiv \sum_{\vec{k}} E_{v_f}(\vec{k}) \exp[-(\vec{k}-\vec{k_0})^2/\sigma^2] \tag{10}$$

The sum is taken over all $\vec{k}$, but only energy values within a few σ of the center point $\vec{k_0}$ contribute significantly to the sum. Note that this total energy includes contributions from background noise, which eventually must be removed in order to make an accurate comparison with the theory.

In Figure 8 we show a plot of $E_{v_f}^T$ as a function of v_f for two values of σ. The solid curve corresponds to $\sigma = 7$, the dashed curve to $\sigma = 10$. The $\sigma = 10$ curve is slightly broader due to the fact that it includes more of the region beyond the center of the swell,
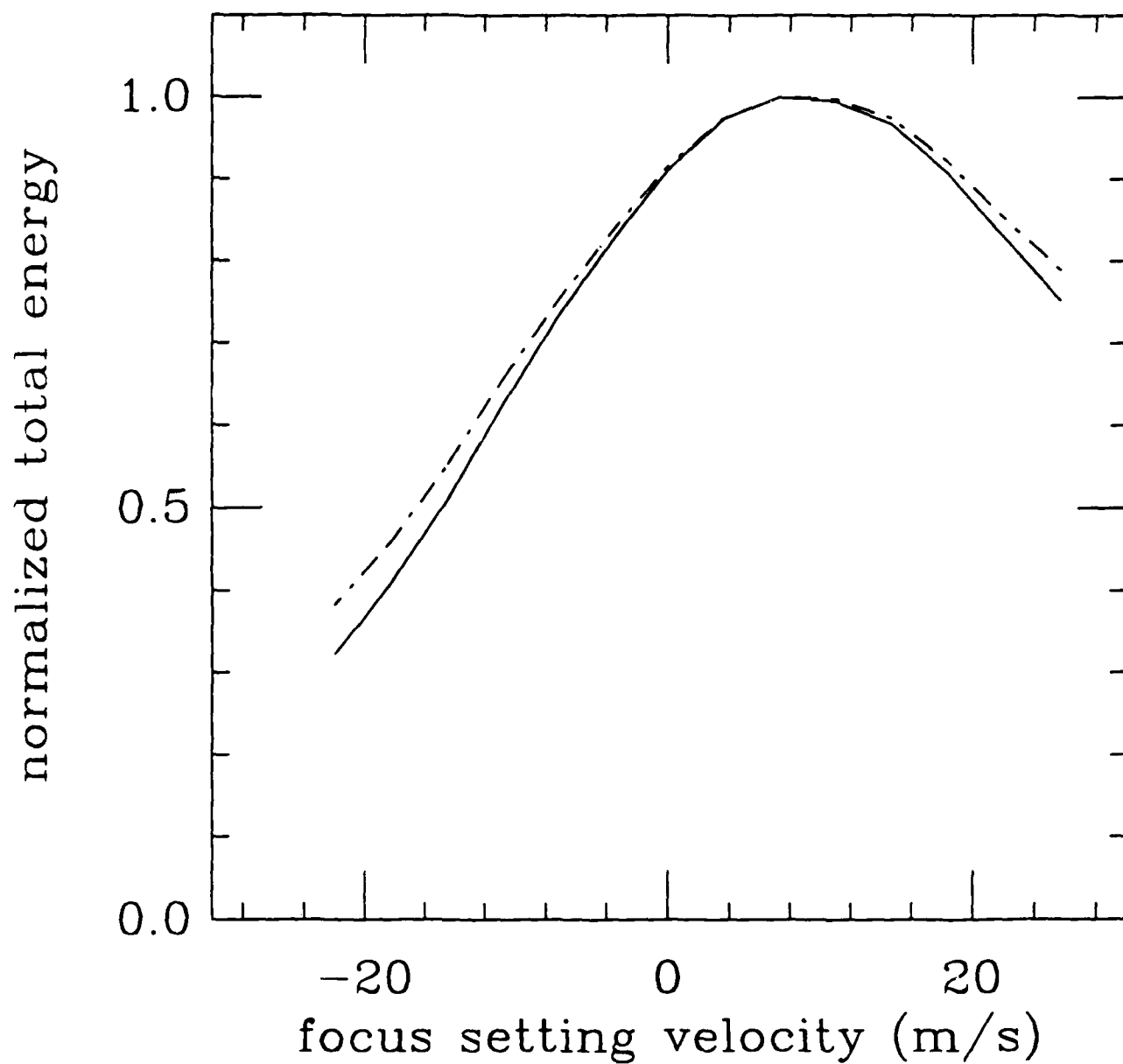
Figure 8. A plot of the total energy as a function of focus-setting velocity for gaussians of different widths. The solid curve uses $\sigma = 7$ and the dashed curve $\sigma = 10$. This represents a factor of two difference in the effective areas covered by the two gaussians.

7-1-'88

which has a weaker signal level and hence a lower signal-to-noise ratio. This lowers the overall signal-to-noise ratio for that curve and so broadens the peak. In either case it is quite clear that the peak of the total energy curve occurs nearest the picture associated with $v_f = 7.3$ m/s.

4.4 Computation of the noise-reduced energy in the swell

The model predicts the focus-setting curve for the case when no noise is present. The effect of adding noise to the spectrum is to broaden the curve while leaving its peak fixed. The precise manner by which this occurs will be made clear later.

We present two different techniques for reducing the noise in the signal and find that both methods give nearly identical results for the case when the signal level is substantially above the background.

The first method obtains an estimate of the noise present in the swell signal by assuming that the The first method obtains an estimate of the noise present in the swell signal by assuming that the noise spectrum is independent of k_x. The noise spectrum would also be independent of k_y except that the data in the y direction has been converted from slant range to ground range. Using this assumption, we pick a region in k-space where there is no discernible signal and filter it with a gaussian of the same radius as that used to compute the weighted total energy. We centered the gaussian at $\vec{k} = (100,0)$ and used $\sigma = 7$ to compute a background noise level. The noise was sampled at $k_y = 0$ in order to avoid problems with the variation of the noise spectrum with k_y. Since the signal is centered near $k_y = 0$, the noise is being estimated at the proper k_y value. This level was then subtracted from the total energy to yield a noise-reduced energy curve. In Figure 9 the total energy is plotted for reference as a dot-dash curve and the noise-reduced energy computing by a straight-forward background subtraction is shown as a solid curve.

The second method, which we call the projection method, assumes that the noise is uniformly distributed in k-space and therefore should be nearly uncorrelated with the signal. We define an inner product on the Fourier-transformed intensities by

$$\langle \tilde{I}_{v_f} | \tilde{I}_{v_f} \rangle \equiv \text{Re} \sum_{\vec{k}} \tilde{I}_{v_f}(\vec{k}) \tilde{I}_{v_f}(\vec{k}) W(\vec{k}) \tag{11}$$
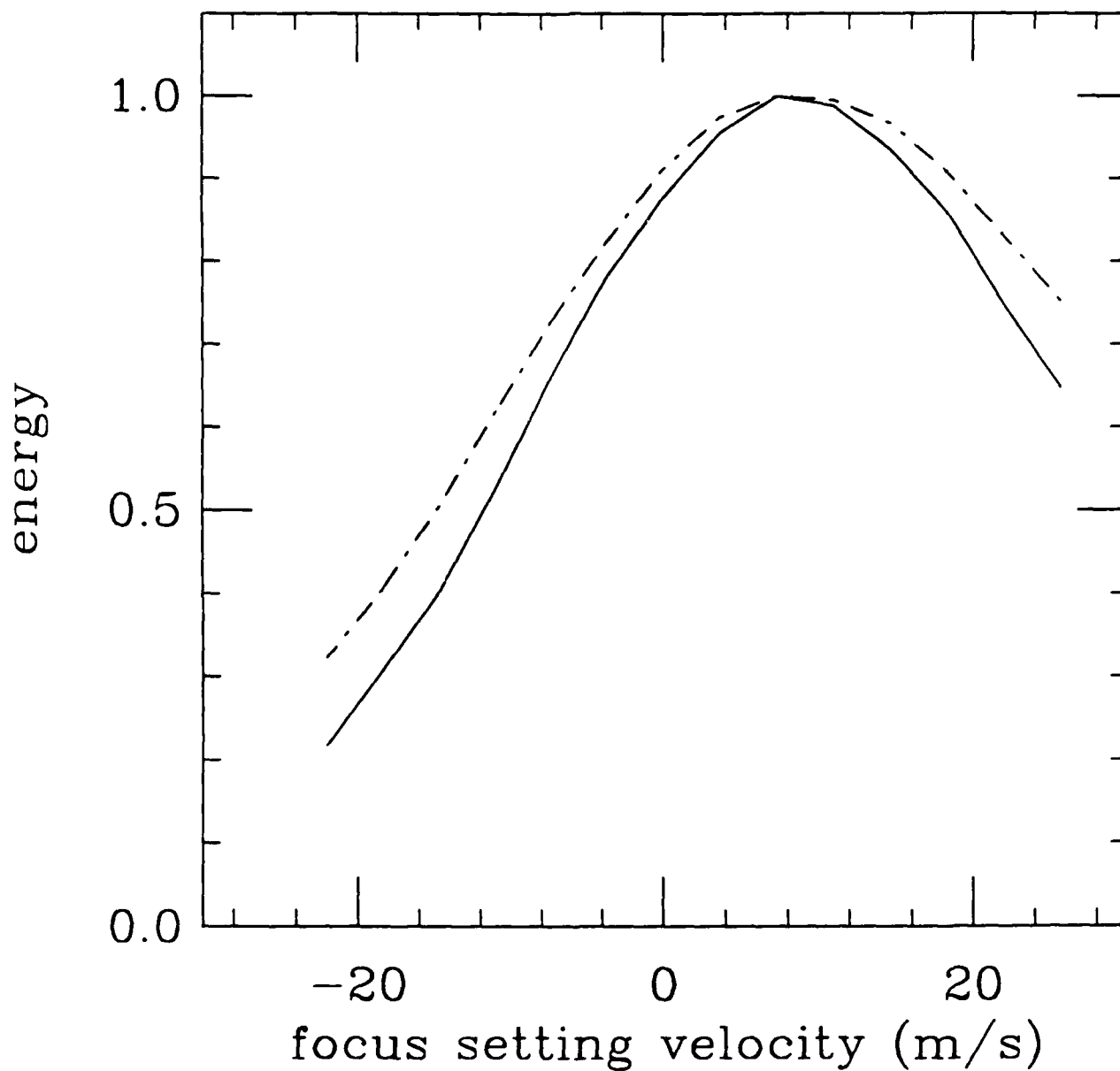
Figure 9. A comparison of the total energy (dashed curve) with the noise-reduced energy (solid curve) as a function of focus-setting velocity. Reducing the noise level in the energy has the effect of reducing the width of the focus-setting curve without altering the peak.

where $W(\vec{k})$ is any real, positive, weighting function that is independent of v_f. We later take $W(\vec{k})$ to be a gaussian centered on the swell just as we did for the computation of the total energy. In using this inner product the transformed intensities are to be thought of as vectors, indexed by $\vec{k}$, in a space whose effective dimensionality is given by the range over which $W(\vec{k})$ is appreciable. Notice that in this inner product space the length of a vector $\tilde{I}_{v_f}$ is just the total weighted energy associated with v_f.

We define the projected energy as

$$E^P_{v_f} \equiv \frac{|\langle \tilde{I}_{v_f} | \tilde{I}_{v_f} \rangle|^2}{\langle \tilde{I}_{v_f} | \tilde{I}_{v_f} \rangle} \tag{12}$$

where v'_f is the focus-setting velocity at which the total energy is maximal. Computation of this projected energy therefore assumes that the computation of enough of the total energy has been performed to establish the optimal focus setting. The intent of the projection method is to reduce the noise in the remaining energy values in order to get an accurate focus-setting curve to compare with the theory.

The method can be understood by considering the following simple model. Suppose that $\tilde{I}$ can be written as a sum of signal and noise contributions:

$$\tilde{I}_{v_f}(\vec{k}) = \tilde{I}^S_{v_f}(\vec{k}) + \tilde{I}^N_{v_f}(\vec{k}) \tag{13}$$

The projection of one $\tilde{I}$ on another is then

$$\langle \tilde{I}_{v_f} | \tilde{I}_{v_f} \rangle = \langle \tilde{I}^S_{v_f} | \tilde{I}^S_{v_f} \rangle + \langle \tilde{I}^S_{v_f} | \tilde{I}^N_{v_f} \rangle + \langle \tilde{I}^N_{v_f} | \tilde{I}^S_{v_f} \rangle + \langle \tilde{I}^N_{v_f} | \tilde{I}^N_{v_f} \rangle \tag{14}$$

If we suppose as a simple model that the vectors $I^S_{v_f}$ and $I^S_{v_f}$ are nearly parallel in the inner-product space (defocusing merely changes the magnitude of each component in k-space by the same factor), that, as a worst case, the vectors $I^N_{v_f}$ and $I^N_{v_f}$ are parallel, and that the contribution due to noise is essentially constant for all v_f, then we can write

$$\langle \tilde{I}^S_{v_f} | \tilde{I}^S_{v_f} \rangle = f(v_f)$$

$$\langle \tilde{I}^S_{v_f} | \tilde{I}^N_{v_f} \rangle = \sqrt{n_0} \cos \theta \tag{15}$$

$$\langle \tilde{I}^N_{v_f} | \tilde{I}^N_{v_f} \rangle = n_0$$

The function $f(v_f)$ is predicted by the theory and decreases on either side of the optimal value v_f', where its value is normalized to 1 for convenience.

Using equations 15, and the assumption that each $\bar{I}^S$ is nearly orthogonal to each $\bar{I}^N$, (that is $\cos \theta = 0$), we obtain for the projected energy

$$E_{v_f}^P / E_{v_f'}^P \approx \frac{(f + n_0)^2}{(1 + n_0)^2} \tag{16}$$

and for the total energy

$$E_{v_f}^T / E_{v_f'}^T \approx \frac{f^2 + n_0}{1 + n_0} \tag{17}$$

both of which are normalized so that their values are 1 at the optimal focus setting. We see that the normalized projected energy is above the actual signal energy but below the total normalized energy by an amount:

$$E_{v_f}^T / E_{v_f'}^T - E_{v_f}^P / E_{v_f'}^P \approx \frac{n_0}{(1 + n_0)^2} (1 - f)^2 \tag{18}$$

In essence, the noise component has been reduced because the total energy is projected onto the vector whose noise component is minimal, instead of onto a vector whose relative noise component grows with increased defocusing.

A good measure of the level of noise remaining in the computed energy is the ratio of the value of the energy for complete defocusing ($f = 0$) to the value at optimal focusing ($f = 1$), which we call ε. The value of ε ranges between 0 and 1, with $\varepsilon = 0$ corresponding to no noise and $\varepsilon = 1$ corresponding to no discernible signal. For the projected energy the value of ε is

$$\varepsilon_P = \left(\frac{n_0}{1 + n_0} \right)^2 \tag{19}$$

while for the total energy the value is

$$\varepsilon_T = \frac{n_0}{1 + n_0} = \sqrt{\varepsilon_P} \tag{20}$$

and so the total energy always has a poorer signal-to-noise resolution than does the projected energy (again, assuming that the orthogonality assumption is valid).

Computed projected energies are shown in Figures 10 and 11. In both cases the solid curve represents the projected energy, with $W(\vec{k})$ taken as a gaussian of the form in equation 10. The gaussian is again centered on the wavenumber (23.1,1.07) in units of Δk and the value of σ is chosen to be 7.

In Figure 10 the dashed curve shows for comparison the value of the background-subtracted energy; this is the same curve as shown in Figure 9. We see excellent agreement between the two methods for this data set.

In Figure 11 we show the projected energy for two different values of σ. The solid curve is for $\sigma = 7$ and the dashed curve is for $\sigma = 5$, which means that the effective area covered by the gaussian associated with the solid curve is a factor of two larger than the area covered by the second gaussian. Nevertheless, unlike the situation with the total energy (see Figure 8), the projected energy is not sensitive to the choice of σ. This gives us confidence that the projected energy curve can be used as a valid comparison to the model predictions for the focus-setting curve.

5. Comparison with Theory

Schult, Henyey, and Wright (1988) make the following theoretical prediction for the normalized signal energy as a function of focus-setting velocity v_f

$$E_{v_f} = \exp\{ -2k_0^2 \Delta T^2 [v_f - (v_\phi + u_x)/2]^2 \} \qquad (21)$$

where k_0 is the wavenumber of the swell, ΔT is a total effective look time, which for the data of this study has the value 0.71 sec, v_ϕ is the phase velocity of the swell, and u_x is the surface current, which could be associated with the orbital velocity of the waves. The effective look time is obtained by taking the nominal look time of 1.74 seconds (Shemdin, 1986, p.83) and dividing it by $\sqrt{6}$ to give the effective look time for a gaussian-profile window. If the waves have an amplitude of $A = 1$ m then the orbital velocity amplitude is $k_0 A v_\phi = 0.7$ m/s. Since this is substantially smaller than the typical phase velocity of these waves, to first order we can neglect the effects of the orbital velocity, which means that we expect the optimal focus-setting velocity to occur at $v_\phi/2$. More detail can be found in Schult, Henyey, and Wright (1988). Since the depth of the water for the data of this study is 60 m and the wavelength of the dominant swell is 121 m, we may use the deep water form of the surface wave dispersion relation to obtain

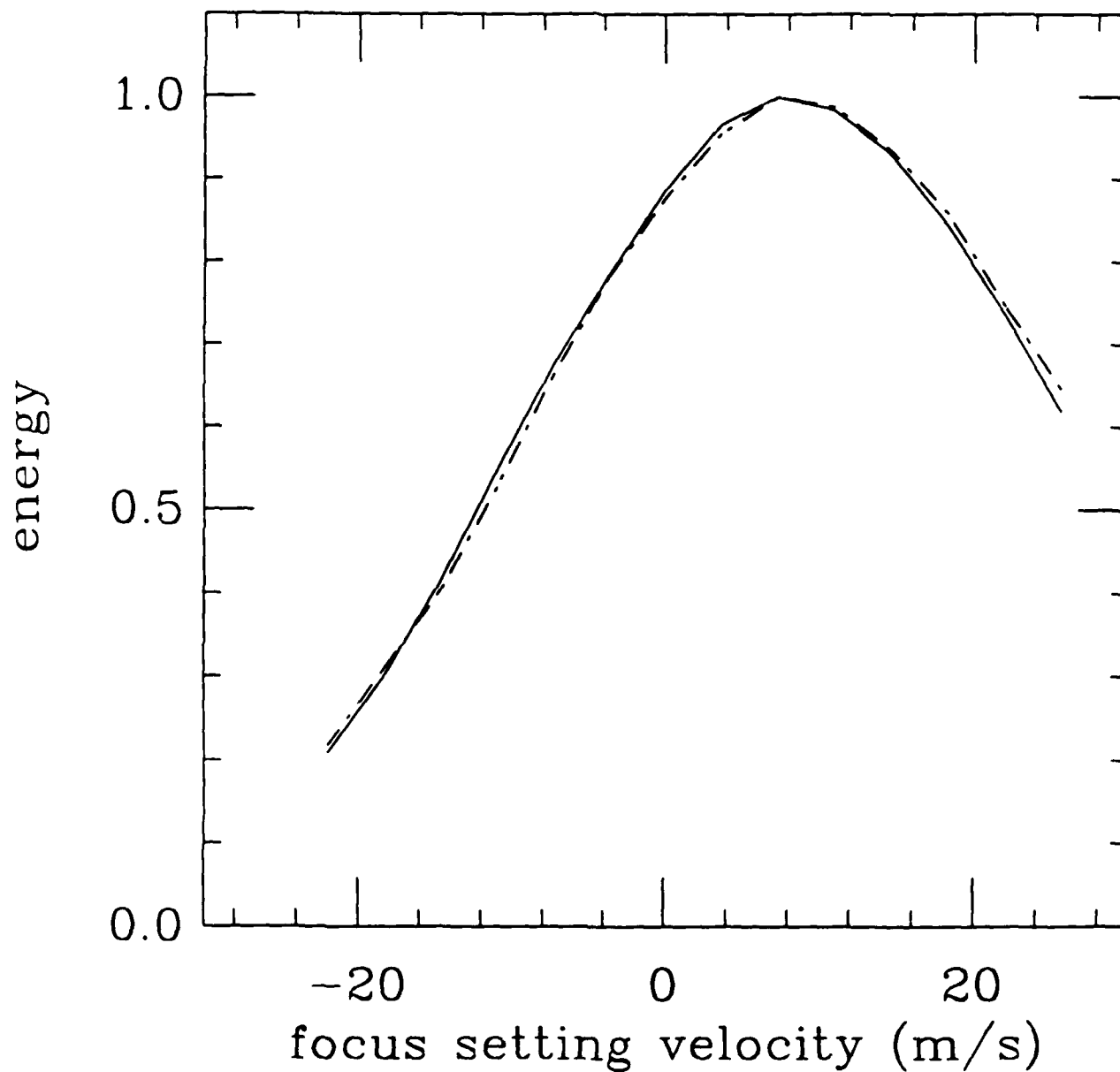$$v_\phi = \sqrt{\frac{g}{k_0}} = 13.8 m/s \qquad (22)$$

Figure 10. A comparison of the noise-reduced energy for the two noise-reduction techniques. The solid curve is the result of the projection technique; the dashed curve is the result of the background-subtraction technique (as in Figure 9).
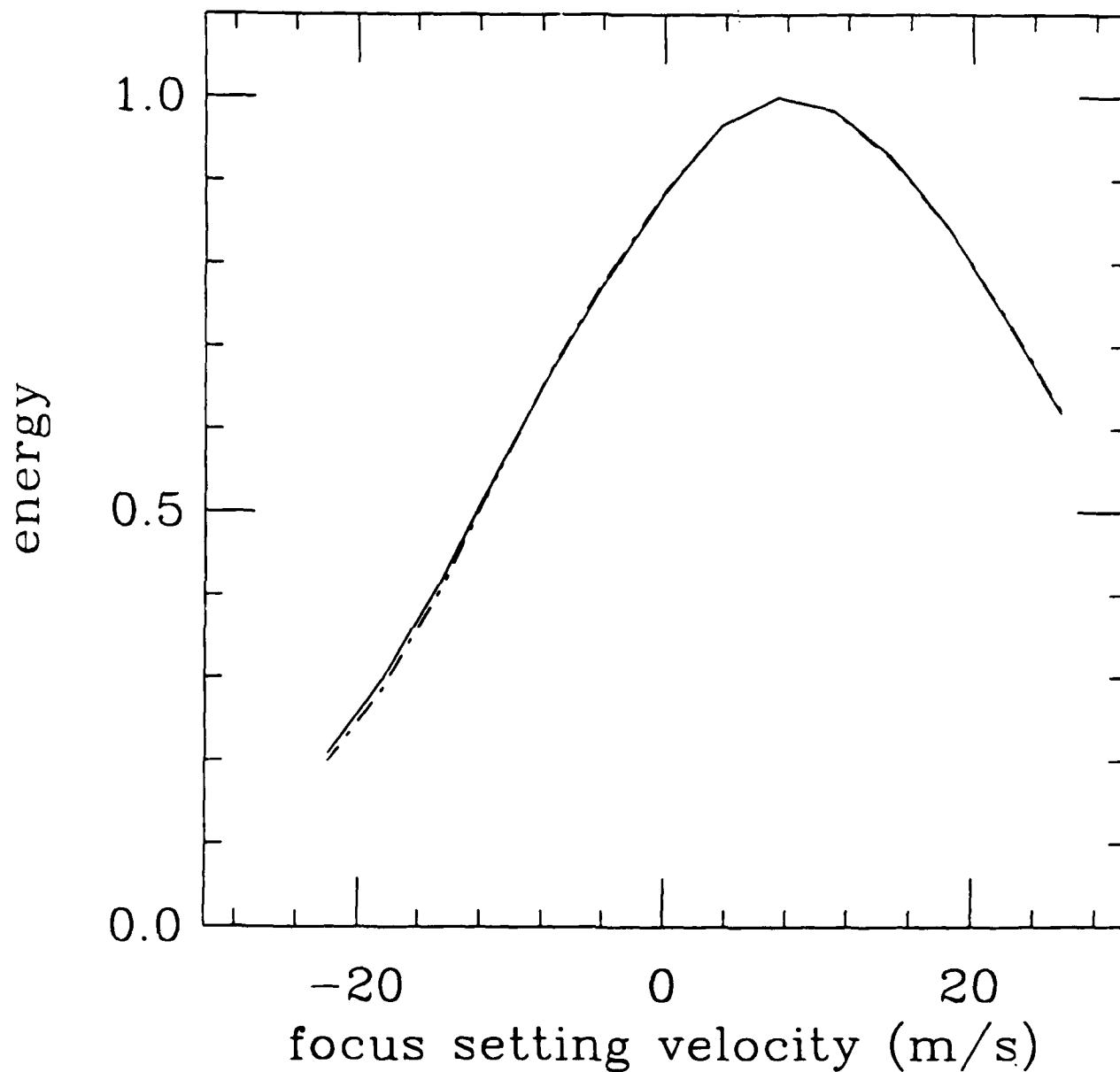
Figure 11. The projected energy for two different values of σ, corresponding to a factor of two difference in the effective areas covered by the two gaussians. We see that, unlike the total energy in Figure 8, the normalized projected energy is not sensitive to the choice of σ.

The model therefore predicts that the optimal focus setting occurs when v_f is $13.8/2 = 6.9$ m/s and that coefficient in the gaussian should have a value of $2k_0^2 \Delta T^2 = 2.66 \times 10^{-3}\, s^2/m^2$.

In Figure 12a we show a plot of the computed project energies (circles) along with the theoretical focus-setting curve (solid curve) for the data of tape AXCMF003. The computed curve shows a maximum at about 8 m/s instead of the predicted 6.9 m/s and the widths of the curves are essentially the same. In Figure 12b we show the same plot for the data of tape AXCMF006, which again is supposed to be identical to the data of tape AXCMF003 except that different focus-setting velocities were sampled. One would expect, of course, that the computed curves should lie on top of each other, and so we are at a loss to explain the discrepancy between the two computed curves. The peak of the computed curve in Figure 12b occurs at about 8.4 m/s, but the width is quite different from either the prediction of the model or the data from the other tape. We have spent some time considering changes in the model that would account for the higher focus-setting velocity and larger width of the data in Figure 12b and have found the predictions of the model to be quite robust. We therefore believe the model prediction to be correct and suggest that additional experimental work will be needed to explain the discrepancies.

Nevertheless, we believe that the calculations presented in both Figures 12a demonstrate that the data does not support the prediction of an optimal focus-setting velocity at either the phase velocity (13.8 m/s) or the orbital velocity of the wave (≤ 0.7 m/s). The model prediction that optimal focusing occurs at just half of the phase velocity is most consistent with the computed focus-setting curves.

6. Comparison with Data from a Lower Height

We also had available a sequence of pictures taken at the same location but about an hour earlier and at an altitude of 20,000 feet instead of 38,000 feet. The data on this tape span the velocity range ± 25.67 m/s, like the data of tape AXCMF006. We analyzed this data in precisely the same manner as that for the earlier data and in this section will compare our results with those obtained for the higher altitude.
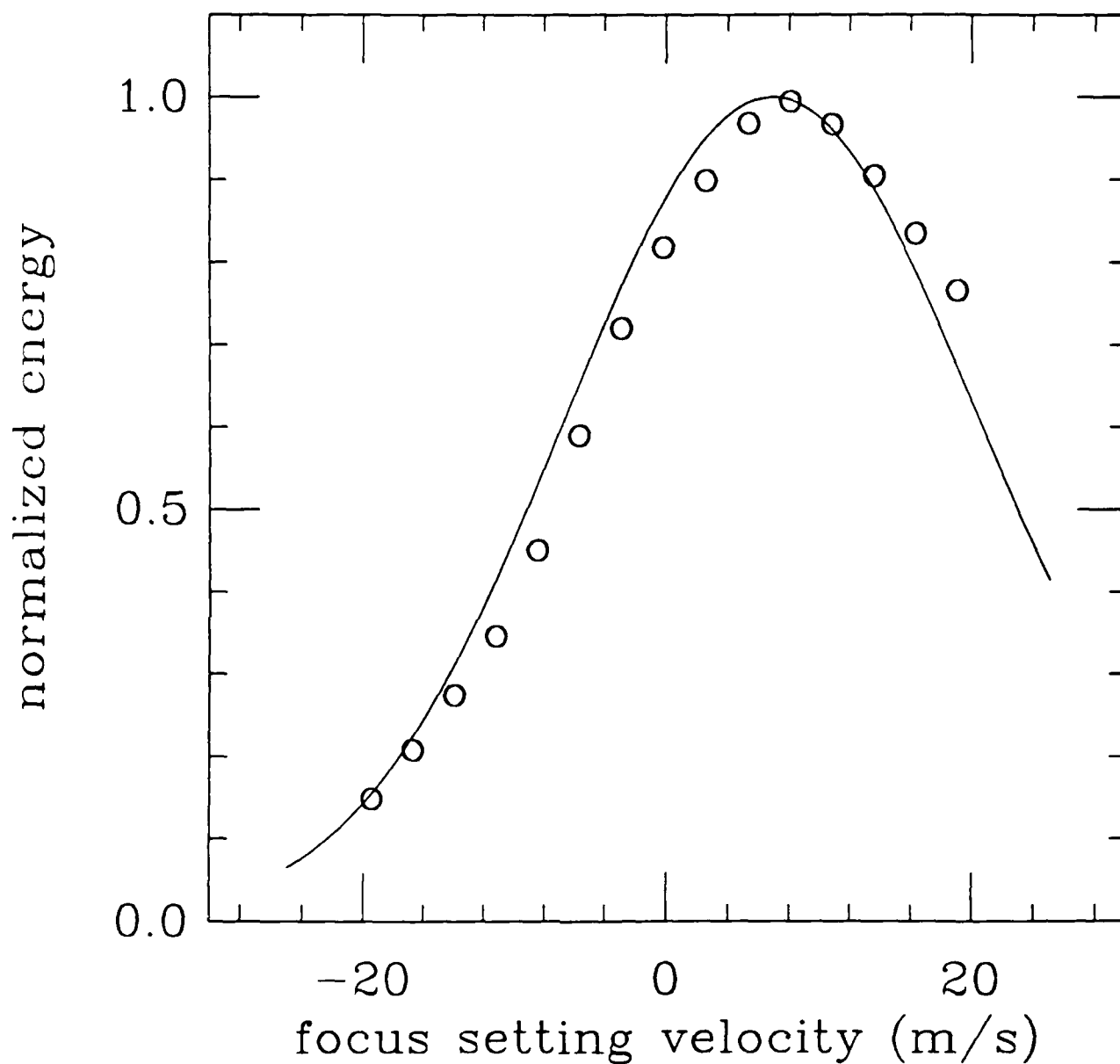
Figure 12a. A comparison of the computed focus-setting curve (circles) with the prediction of the model (solid curve) for tape AXCMF003. The computed curve peaks at nearly half the phase velocity, as predicted by the model, and is good enough to rule out either the phase velocity or the orbital velocity of the waves as the velocities of optimal focus.
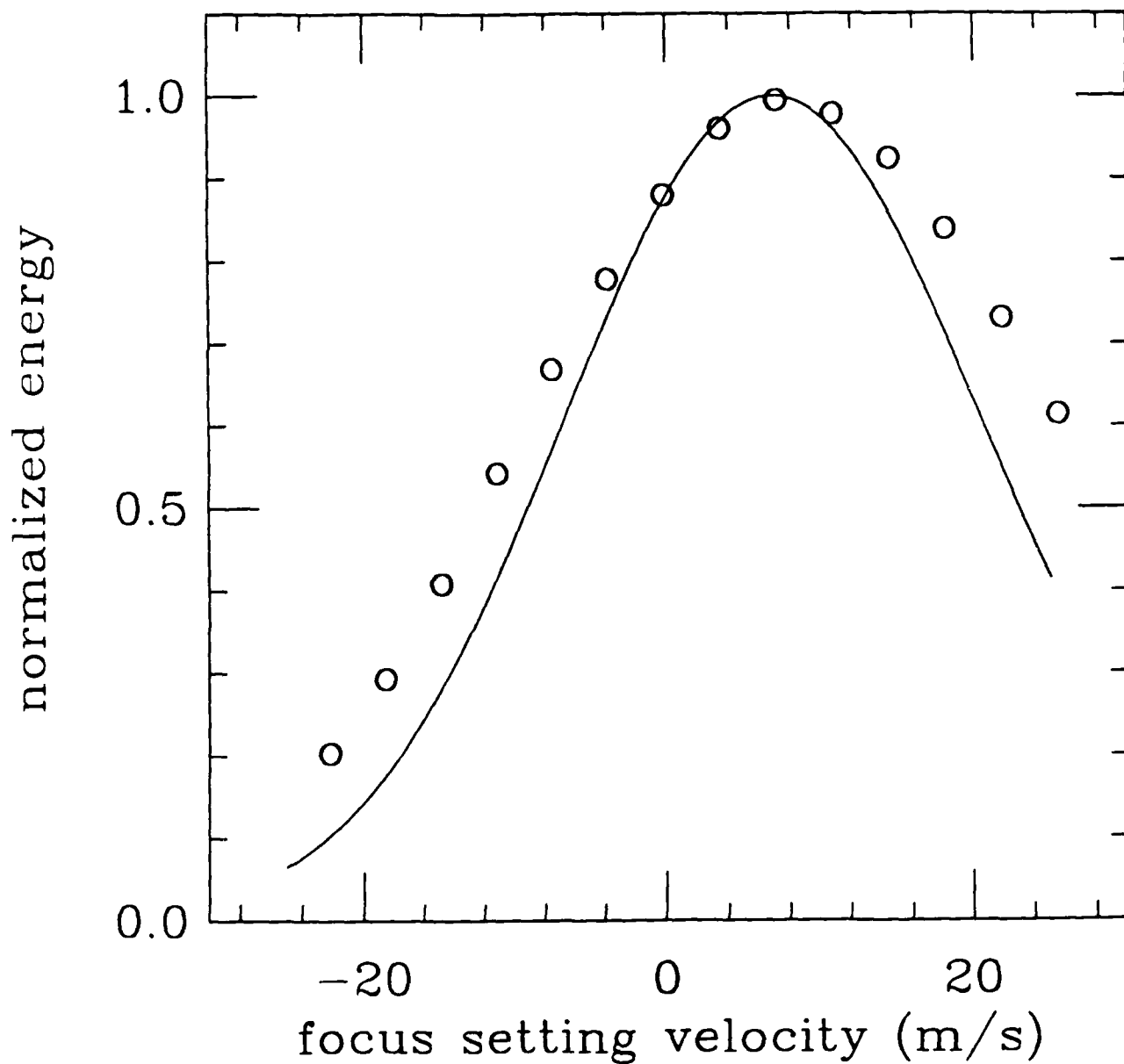
Figure 12b. A comparison of the computed focus-setting curve (circles) with the prediction of the model (solia curve) for tape AXCMF006. The computed curve peaks at nearly half the phase velocity, as predicted by the model, and is good enough to rule out either the phase velocity or the orbital velocity of the waves as the velocities of optimal focus.

Figure 13 shows the gray-scale plot of the Fourier transform for this picture, which is to be compared to Figure 5 for the higher altitude. In comparing the two it is immediately obvious that there is substantially less swell present around the region $\vec{k} = (21, 1)$ than in the original data set. Also evident in this figure is a large swell component located roughly along the direction -45 degrees (with positive k_y downward).

We computed the average $\vec{k}$ as before, with the same restrictions ($16 \leq k_x \leq 30$ and $-6 \leq k_y \leq 8$), and obtained a value of (23.4,1.08), to be compared with the value (23.1,1.07) obtained from the first data set.

To produce a focus-setting curve for the lower altitude we note that the equation for the optimal resolution of the SAR processing is

$$Res = \frac{\lambda}{2} \frac{1}{\Delta T} \frac{R}{v} \tag{23}$$

where λ is the wavelength of the radar, ΔT is the look (integration) time, R is the range and v is the velocity of the aircraft. In the TOWARD experiment the look angle was fixed for all flights, as was the resolution (Howard Zebker, JPL, private communication), which means that the look time is directly proportional to the altitude of the flight. Since the effective look time for our model is 0.71 sec for an altitude of 38,000 feet, the look time for 20,000 feet is 0.37 sec. The focus-setting curve is shown in Figure 14. The circles in the figure represent the computed projected energies and the solid curve represents the theoretical prediction. We checked the background-subtraction method against the projection method for this case and found that the two methods were in good agreement on low-velocity side of the peak but that the projection method was far superior in eliminating noise on the high-velocity side.

The peak of the computed curve shown in Figure 14 is consistent with the peak of the curve in Figure 12b, which occurs at about 8.4 m/s.
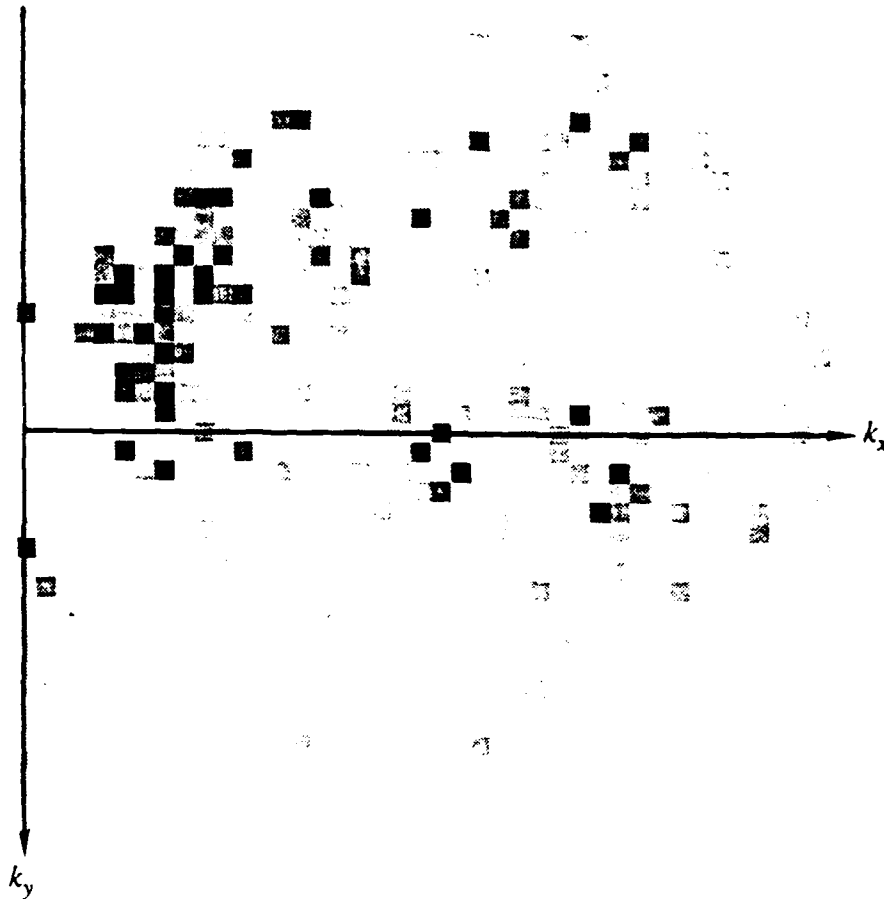
Figure 13. The two-dimensional spectrum of the data set taken in Leg 1 at 20,000 feet. There is substantially less of the swell centered around $(21,1)\Delta k$ in this spectrum and correspondingly a lower signal-to-noise rather for this region. There is also a much larger signal in the direction at roughly -45 degrees.
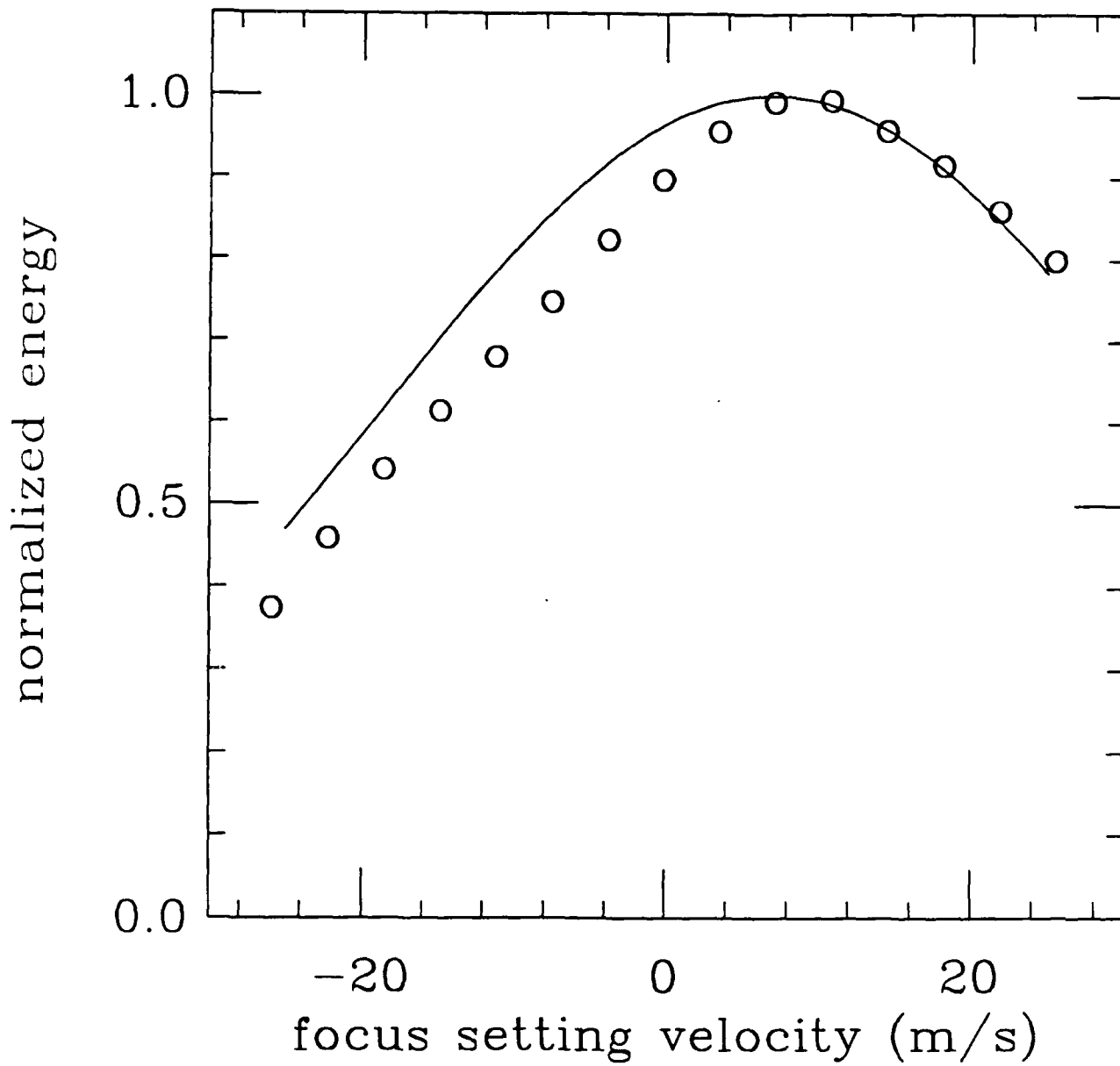
Figure 14. A comparison of the computed focus-setting curve (circles) with the model prediction (solid curve) for the second data set.

7. Summary and Conclusions

In this paper we have analyzed data from the TOWARD experiment in order to make comparisons between the theoretical focus-setting curves predicted by the model of Schult, Henyey, and Wright (1988) and actual curves computed from SAR data. We have shown that the computed curves are good enough to distinguish between different models for SAR imaging of time-dependent surfaces, ruling out either the phase velocity or the orbital velocity alone as the proper focus-setting velocity for SAR imaging. Instead, the model prediction of an optimal focus-setting velocity at just half of the phase velocity of azimuthally-directed waves is highly favored.

We have also demonstrated that proper spectral processing of the SAR data can greatly enhance the computed focus-setting curves. The sources of the spectral activity have been identified as the open regions between local islands. Selecting a region of k-space associated with the signal of interest both guarantees that all important components of the signal are included in the focus-setting curve. We have demonstrated that a substantial amount of the dominant swell can be lost if the direction of the swell is assumed from the intention of the experiment rather than determined numerically from the data set itself.

Use of a 2-D spectrum also provides a mechanism for reducing the background noise contribution to the focus-setting curve. We have shown that the projection method can be used to eliminate noise from the desired signal, but that it requires the inclusion of a number of Fourier components in order that the statistical orthogonality of signal and noise be valid.

We are at a loss to explain the discrepancies in the computed curves shown in Figures 12a and 12b, which purportedly represent exactly the same experimental situation. Whereas the width of the curve in the first figure is in good agreement with the model prediction, the second computed curve is substantially broader than one would expect. In testing a number of possible corrections to the model, we have found the predictions of the model to be quite robust, and therefore believe that the model predictions are correct; we further believe that future experimental data will resolve the discrepancies.

Acknowledgements

References

R.L. Schult, F.S. Henyey, and J.A. Wright, Imaging of Ocean Waves by SAR, LJI-87-P-467, 1980. (Submitted for publication).

O.H. Shemdin, TOWARD Field Experiment Interim Report-Volume I: Data Summary and Early Results, May, 1986.

Edmond K. Tajirian, TOWARD Multifocus Processing of L-Band SAR Images, Ocean Research and Engineering Report No. ORE 87-1, 1987.